Liver International ISSN 1478-3223

BASIC STUDIES

A comprehensive gene expression analysis of human hepatocellular carcinoma cell lines as components of a bioartificial liver using a radial flow bioreactor

Makoto Kosuge[1,2], Hiroko Takizawa[2], Haruka Maehashi[3], Tomokazu Matsuura[4] and Senya Matsufuji[2]

1 Department of Surgery, The Jikei University School of Medicine, Tokyo, Japan
2 Department of Biochemistry II, The Jikei University School of Medicine, Tokyo, Japan
3 Department of Biochemistry I, The Jikei University School of Medicine, Tokyo, Japan
4 Department of Laboratory Medicine, The Jikei University School of Medicine, Tokyo, Japan

Keywords
bioartificial liver – gene expression analysis – hepatocellular carcinoma – human cell line – microarray – radial flow bioreactor

Correspondence
S. Matsufuji, MD, PhD, Department of Biochemistry II, The Jikei University School of Medicine, 3-25-8 Nishi-shinbashi, Minato-ku, Tokyo 105-8461, Japan.
Tel: +81 3 3433 1111
Fax: +81 3 3436 3897
e-mail: senya@jikei.ac.jp

Received 13 May 2005
accepted 2 October 2006

DOI:10.1111/j.1478-3231.2006.01410.x

Abstract

Background/Aims: The cells constituting a bioartificial liver are crucial for an effective liver support system. We compared global gene expression profiles in a radial flow bioreactor or a monolayer culture of three functional liver cell lines previously established from human hepatocellular carcinoma. *Methods:* The expressions of 60 000 genes of the FLC-4, FLC-5, and FLC-7 cell lines were analyzed by the microarray technique with the Affymetrix GeneChip system. Global gene expression profiles were compared with two-way cluster analysis. Several liver function-related genes were compared between the bioreactor and culture conditions. *Results:* Cluster analysis revealed that gene expression profiles of bioreactor-grown cells resembled those of the normal liver. Genes related to cellular structure were highly expressed in the bioreactor-grown cells, while genes involved in proliferation or carcinogenesis were suppressed. In the bioreactor-grown cells, some genes for liver functions were expressed at a level similar to that in normal liver, although none of the cell lines expressed the complete set of genes encoding ammonium metabolism or cytochrome P450 species. *Conclusion:* The high-density three-dimensional culture in the radial flow bioreactor prompted differentiation of the cells. These data may be useful for improving the cells by genetic or pharmacological reinforcement and for monitoring bioartificial livers.

Liver transplantation has been the most effective therapy for hepatic failure, a major cause of death from liver diseases. However, insufficient numbers of equipped facilities and donor organs, together with the ethical issues involved, pose fundamental problems. It is therefore necessary to develop effective alternatives, and one promising approach is the temporary use of a bioartificial liver (BAL) that provides a substitute for the organ until tissue regeneration or a donor liver is obtained (1).

From a practical perspective, cells constituting a BAL are crucial (2). Cells most widely and successfully used are primary hepatocytes from human embryos or other mammalian organisms (3, 4), as well as cell lines established from human hepatocellular carcinoma. Rozga and colleagues (5, 6) reported that porcine hepatocytes cultured in a hollow fiber-type reactor improved clinical conditions in patients with liver failure. Sussman et al. (7) and Yamashita et al. (8) demonstrated that a BAL with human hepatoblastoma cell culture is effective in hepatitis treatment. On the other hand, several problems have been found in the application of BAL, including (i) difficulty in maintaining the cell cultures for a long period of time without losing physiological liver functions, (ii) insufficiency in cell supply, (iii) difficulty in scaling up BAL, (iv) secretion of proteins in unknown quantities and inappropriate profiles, and (v) the presence of various known and unknown infectious agents. Thus, a standard choice for cells constituting BAL has not been established (9, 10). Previously, Fujise et al. (11) reported the use of several cell lines derived from human hepatocellular carcinoma. Some of these have been further characterized and named FLC (functional liver cells). Because these cell lines preserve many physiological liver functions, we regarded them as a

potential component of a BAL that would solve several of the aforementioned problems. However, to apply these cells to a BAL, it is necessary to evaluate their physiological characteristics and to determine their most appropriate culturing conditions.

It has been suggested that the function of cultured hepatocytes may improve when they are grown in a three-dimensional (3D) culture, not as a monolayer, because 3D culture conditions more closely resemble the normal tissue environment than those of culture dishes. To create 3D culture conditions, we used a radial-flow bioreactor (RFB), a cylindrical culturing reactor filled with a matrix. The medium is pumped from the periphery toward the reactor center with an increasing rate, sufficiently supplementing the cells with oxygen and nutrients. The matrix consists of porous beads with a high pore density, allowing for a large surface attachment area and reduction of shear force caused by direct flow of the medium toward the cells. In addition, the use of porous hydroxyapatite beads, which have good cell adaptation, improved the attachment and functionality of hepatocellular carcinoma cells (12). This system allows a cell density 10 times higher than that obtained in an average hollow-fiber culture and 100 times higher than that obtained in floating cell culture systems. Application of this system integrated into extracorporeal circulation for patients with liver failure is now under investigation. This new BAL also provides a suitable experimental system for studies on drug metabolism, mechanisms of viral infections, and liver physiological functions (12–14).

In the present study, we used the Affymetrix GeneChip technology to analyze comprehensively the global gene expression profiles of three FLC lines (FLC-4, FLC-5, and FLC-7) (11), and compared changes in the expression profiles brought about by different culture conditions, namely the RFB condition and a standard monolayer condition on culture dishes. The purpose of this study was to gain new insights into the genetic and pharmacological features of cells or identification of functional cells for BAL support. In addition, we aimed to produce a gene expression database not only for selection of the most therapeutically appropriate cells but also for further analysis of cell function reinforcement techniques that would facilitate generation of a highly functional BAL.

Materials and methods

Cell lines

Development of FLC-4, FLC-5, and FLC-7 cell lines (previous names, JHH-4, JHH-5, and JHH-7) from hepatocellular carcinomas of Japanese patients has been published (11). The cells have been adapted to be able to grow in serum-free medium, preserving their liver-specific functions. The human hepatoblastoma cell line HepG2 (ATCC no. HB-8065) was obtained from the American Type Culture Collection (ATCC; Manassas, VA).

Cell culture

Monolayer culture

FLC-4, FLC-5, and FLC-7 cells were maintained in ASF104 serum-free medium (Ajinomoto Co. Ltd., Tokyo, Japan) in 175 cm^2 culture flasks (Falcon, Becton-Dickinson, Franklin Lakes, NJ) as described previously (13). Cells were inoculated into 100 mm culture dishes (Corning, Corning, NY) at a density of 5% confluency and cultured with medium changes every 3 days. When the cells grew to confluency, the medium was changed again and the culture was continued for an additional 24 h before harvesting. HepG2 cells were grown in Dulbecco's modified Eagle's medium (DMEM, Nissui Pharmaceutical Co. Ltd., Tokyo, Japan) with 10% fetal bovine serum (JRH Biosciences, Lenexa, KS) in 100 mm cell culture dishes until 50% confluency. The medium was then changed to ASF104 serum-free medium. After 3 days of culture, the medium was changed again to a fresh ASF104 serum-free medium and cells were cultured further for 24 h. All cell cultures were carried out under a constant temperature of 37 °C with highly humidified 95% air and 5% CO_2.

Radial flow bioreactor culture

An RFB (400 ml, ABLE Co. Ltd., Tokyo, Japan) (13) was filled with hydroxyapatite ceramic beads (diameter 1–2 mm, pore size $< 200\,\mu m$, PENTAX, Tokyo, Japan). FLC-4, FLC-5, or FLC-7 cells maintained in ASF104 serum-free medium were recovered from culture flasks with trypsin-EDTA, and approximately 1×10^9 cells were transferred to the RFB from the inlet tube. Cell growth was monitored by measuring oxygen consumption with an oxygen electrode (13). After growing to confluency, the cells were cultured for a few additional days (the total culture period in the RFB was 10–14 days).

RNA sample isolation

For monolayer cultures, the medium was removed by aspiration. The cells were washed twice with cold phosphate-buffered saline and maintained at − 80 °C

Liver International (2007)

in culture dishes until use. Cells cultured in the RFB were recovered as stuck to the beads after drainage of the medium and collected into 2 ml cryotubes without washing to be kept in liquid nitrogen.

Total RNA was extracted using RNAzol™ B solution (TEL-TEST Inc., Friendswood, TX). Monolayer cultured cells were lysed by adding 2.5 ml solution/10 mm dish and pipetting a few times. The RFB-cultured cells attached to ceramic beads were transferred from cryotubes into 15 ml tubes and lysed following the addition of RNAzol™ B (5 ml/1.5 ml beads), followed by vigorous shaking with a vortex mixer. For both cases, the lysates were collected into 15 ml tubes and 0.1 volume of chloroform–isoamyl alcohol (49:1) solution was added. The mixtures were then shaken, kept on ice for 5 min, and centrifuged at 12 000g at 4 °C for 30 min. Upper aqueous phases were transferred into fresh tubes and equal volumes of isopropanol were added. The solutions were mixed by inverting several times and kept on ice for 15 min. After a 30-min centrifugation at 12 000g (4 °C), the supernatants were discarded. RNA pellets were washed with 75% ethanol, air dried, and dissolved in diethylpyrocarbonate (DEPC)-treated water. Poly $(A)^+$ RNA was isolated from the total RNA using the Micro-FastTrack 2.0 Kit (Invitrogen, Tokyo, Japan). As a control, poly $(A)^+$ RNA from normal human livers (a pool of four men and women, ages 44–50, Clontech, Tokyo, Japan) was used.

Microarray analysis

Biotin-labeled cRNAs were synthesized according to the instructions for Affymetrix GeneChip Expression Analysis. Briefly, double-strand cDNA was synthesized from the isolated poly $(A)^+$ RNA by Superscript II reverse transcriptase (Invitrogen) and T7-$(dT)_{24}$ primer (Amersham Bioscience, Tokyo, Japan). The cDNA was then transcribed *in vitro* to cRNA with biotinylated dUTP and dCTP using the Enzo BioArray High Yield RNA Transcript Labeling Kit (Amersham Bioscience). After purification with the RNeasy Mini Kit (Qiagen, Valencia, CA), cRNA was fragmented with the fragmentation buffer (40 mM Tris-acetate, pH 8.1, 10 mM potassium acetate, 30 mM magnesium acetate). The fractionated cRNA (12.5 μg) was hybridized with each Gene Chip Human Genome Array (U95; chips A, B, C, D, and E; Affymetrix, Santa Clara, CA). Array A contained probes for approximately 12 000 already known genes and arrays B–E total of almost 48 000 EST probes. Following washing and staining, the microarrays were scanned using a Gene Array Scanner (Hewlett Packard Co., Palo Alto, CA). Gene expression levels were calculated from the scanned images with the Microarray Suite and Data Mining Tools software (Affymetrix), giving single average difference ratios across probe pairs as well as reliability scores [absent (A), present (P), or marginal (M) based on the variability of hybridization with each probe set]. The Gene Spring software (Silicon Genetics, San Carlos, CA) was used for data analysis. A two-way cluster analysis (15) was carried out on the data from arrays A–E and eight samples (FLC-4, -5, and -7 each under RFB and monolayer cultures, HepG2, and normal human liver). To compare expression levels of each gene between the samples, values of average differences after normalization were used.

Results

Global analysis of gene expression in FLCs under different culture conditions

The global gene expression profiles were compared among the three FLC lines, each under 3D and monolayer culture conditions, HepG2 under monolayer condition, and normal liver. Cluster analysis revealed that FLC-4 grown in the RFB had the closest expression profiles to the normal liver, whereas the gene expression profiles of FLC-4 and FLC-7 grown in monolayer cultures were the most different (Fig. 1). In addition, the gene expression profiles of FLC-4 and FLC-7 had a closer resemblance to that of the normal liver in the RFB culture compared with those in the monolayer condition; such a change was not obvious for FLC-5.

Next, we surveyed genes for which expression levels were commonly higher or lower for all three cell lines when cultured under the RFB condition than those under the monolayer conditions (Table 1). Only three common genes of the three FLC lines were found to have higher expression levels (more than threefold) in RFB, as compared with the monolayer cultures (Table 1, with asterisks). On the other hand, no genes showed commonly lower expression levels (more than threefold) in RFB compared with monolayer cultures among the three cell lines. We also examined common changes in gene expression only for FLC-4 and FLC-7 because, as shown in Fig. 1, the response of FLC-5 to cell culture conditions was substantially different from those of the other two FLC lines. These two cell lines shared 28 and 17 genes, whose expression levels were higher and lower under the RFB condition, respectively (Table 1).

The results of the gene expression analysis are available as a Microsoft Excel® file upon request to the corresponding author.

Table 1. Genes whose expression was commonly changed in the FLC lines between culture conditions. (A) Genes with more than a threefold increase in expression levels under the RFB condition. (B) Genes with more than a threefold decrease in expression levels under the RFB condition.

Function	Symbol	Gene	Accession no.	FLC-4	FLC-5	FLC-7
(A)						
Metabolism	*UGT2B7	UDP glycosyltranferase 2 family, polypeptide B7	J05428	7.11	3.76	5.41
	ALDH1A1	Aldehyde dehydrogenase 1 family, member A1	K03000	3.27	1.59	3.76
Membrane proteins	*JAK1	Janus kinase 1 (a protein tyrosine kinase)	AL039831	3.69	4.59	3.71
	*ATP1B1	ATPase, Na+/K+transporting, β 1 polypeptide	U16799	7.5	5.87	4.37
	CLTB	Clathrin, light polypeptide (Lcb)	M20470	6.2	1.37	10.31
	LAMP2	Lysosomal-associated membrane protein 2	X77196	3.24	2.31	4.37
Cell adhesion	GPR56	G protein-coupled receptor 56	AJ011001	7.61	0.96	10.64
	CD151	CD151 antigen	D29963	6.79	ND	3.78
Cell structure	FLNA	Filamin A, α (actin-binding protein 280)	AL050396	10.28	ND	13.73
	DSTN	Destrin (actin-depolymerizing factor)	S65738	6.66	1.44	3.44
	KRT18	Keratin 18	M26326	3.1	0.9	4.83
Apoptosis	TSSC3	Tumor-suppressing subtransferable candidate 3	AF001294	4.14	0.4	5.2
Transcription	TCF8	Transcription factor 8 (represses interleukin 2 expression)	D15050	3.03	2.3	3.01
Chromosome	CHD4	Chromodomain helicase DNA-binding protein 4	X86691	7.3	1.65	3
	H2AFO	H2A histon family, member O	L19779	3.752	1.75	3.53
(B)						
Metabolism	PAH	Phenylalanine hydroxylase	U49897	4.28	0.23	5.26
	MPI	Mannose phosphate isomerase	X76057	12.3	0.68	3.04
	FABP1	Fatty acid-binding protein 1, liver	M10050	129.89	0.42	21.24
	DDC	Dopa decarboxylase (sromatis L-amino acid decarboxylase)	M76180	5.64	0.84	3.11
Plasma protein	G3A	Apolipoprotein M	AJ245434	10.29	1.54	5.65
	AFP	α-fetoprotein	J00077	65.11	0.31	4.81
	F2	Coagulation factor II (thrombin)	J00307	49.43	2.2	3.26
	AHSG	α2-HS-glycoprotein	M16961	10.93	0.99	14.09
	SERPINA6	α1 antitrypsin, member 6	J02943	6.2	0.52	3.09
Oncogenesis	RGS2	Regulator of G-protein signalling 2	L13463	7.15	0.84	7.8
Tumor suppressor	NDRG1	N-myc downstream regulated gene 1	D87953	5.55	0.17	4.49
MAP kinase inhibitor	DUSP5	Dual specificity phosphatase 5	U15932	4.17	ND	4.86
	DUSP6	Dual specificity phosphatase 6	AB013382	3.77	2.37	3.01
Membrane protein	LGALS3	Lectin, galactoside-binding, soluble, 3 (galectin 3)	AB006780	6.2	0.35	3.34

Asterisks before the gene symbol indicate commonly increased genes in all the three FLC lines. Genes without an asterisk changed commonly only in FLC-4 and FLC-7. Each value represents the change in fold (RFB/monolayer). ND, not determined due to an absence of the transcript in at least one of the pair samples

Differences in albumin/α-fetoprotein expression ratio

As a parameter that reflects the differentiation status of hepatocytes, the ratio of albumin gene expression to α-fetoprotein (AFP) gene expression was calculated from the Gene Chip data (Fig. 2). FLC-4 displayed a markedly higher ratio under the RFB condition (16.8 for the RFB culture vs. 0.28 for the monolayer culture). The ratio for FLC-7 also increased from 0.30 (monolayer) to 1.05 (RFB); however, this increase was not as notable as in FLC-4. On the contrary, FLC-5 demonstrated a decrease in the ratio value: 0.68 for RFB and 1.50 for monolayer culture. Albumin/AFP ratios of the three FLC lines grown under RFB or monolayer conditions were higher than that of monolayer-cultured HepG2.

Liver-specific function

Expression of the genes related to liver functions was compared between each FLC cultured in RFB and the normal human liver (Fig. 3). For AFP, which is not expressed in the normal human liver, the expression level in HepG2 grown on dishes was used as a reference. The expression levels of the albumin gene in all RFB-grown cells were approximately 20–30% of the normal liver (Fig. 3A). FLC-5 and FLC-7 retained

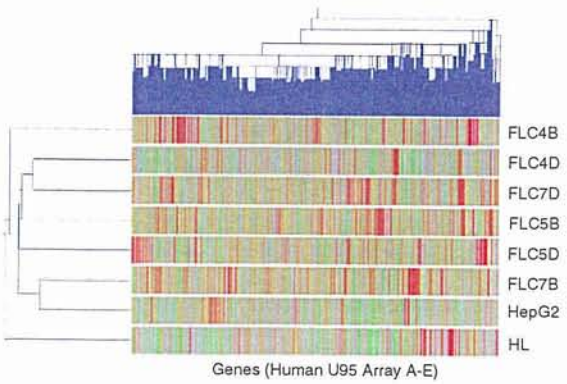

Fig. 1. Cluster analysis of global gene expression. Gene expression of FLC-4, FLC-5, and FLC-7, each cultured in a radial flow bioreactor (B) or cultured on dishes (D), were compared with Affymetrix Human U95 Arrays A–E. RNA samples from HepG2 cultured on dishes and from normal human liver tissue were also analyzed as controls. Red color indicates a relative increase and green color relative a reduction in expression levels. HL, normal human liver.

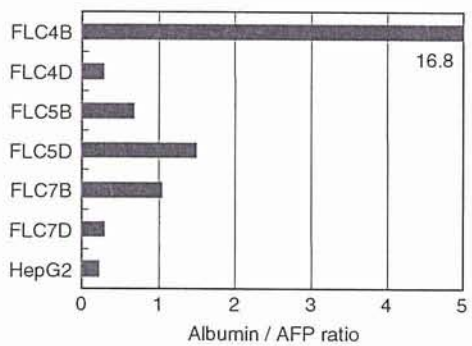

Fig. 2. Ratio of albumin gene expression to α-fetoprotein (AFP) gene expression. FLC-4, FLC-5, and FLC-7, each cultured in a radial flow bioreactor (B) or cultured on dishes (D), were compared. HepG2 cells cultured on dishes were used as a control.

expression of most of the other serum protein genes. However, FLC-4 did not express genes for some serum proteins such as transferrin and α1-antichymotrypsin. Regarding blood coagulation factors, genes for fibrinogen β chain, factor V, and factor X were expressed in all cells, but fibrinogen α chain and factors II, VII, and VIII showed large variations (Fig. 3B). Factor VII gene was detected in FLC-5 and FLC-7, but not in FLC-4 and HepG2, whereas Factor XIII was expressed only in FLC-4. Genes for isoforms of cytochrome P450 (CYP), a representative drug-metabolizing enzyme in the liver were expressed very differently in each FLC line (Fig. 3C). Expressions of CYP51 in FLC-4 and CYP1B1 in FLC-5 were higher than those in the normal liver. FLC-5 also expressed CYP2B and CYP51 in levels comparable with those in the normal liver. CYP1B, 2C9, 2E1, 2J2, and 4F2 are expressed only in one or two FLC lines. The enzymes operating the ornithine cycle are thought to be important for a functioning BAL. Unexpectedly, none of the FLCs expressed all five enzymes (Fig. 3D). The rate-limiting enzymes for the ornithine cycle, carbamyl phosphate synthetase I (CPS I), and ornithine transcarbamylase (OTC) were found not to be expressed at all. Finally, we examined genes for liver-enriched transcription factors hepatocyte nuclear factor (HNF)-1β, HNF-3α, and HNF-3β (Fig. 3E). In all of the FLC lines, the expression levels of HNF-1β were almost comparable with that of the normal liver, and those of HNF-3α and HNF-3β genes were the same or even higher as compared with normal liver. However, no expression of the HNF-4 (α+β+γ) gene was detected in all of the FLCs.

Discussion

The cluster analysis of global gene expression revealed that FLC-4 grown in RFB had the closest gene expression profiles to those in normal liver, and those of FLC-4 and FLC-7 in monolayer cultures were most different (Fig. 1). In general, a tendency toward normal liver gene expression profiles was observed when cells were grown in the RFB compared with monolayer culture conditions.

The GeneChip analysis picked up several genes whose expressions were remarkably altered according to culture conditions. The genes highly expressed in the RFB were mostly those related to cell and tissue structure, encoding proteins for building cellular framework and cellular adhesion. One such protein, filamin Aα (FLNA), is an actin filament bridging protein that promotes orthogonal branching of actin filaments, links actin filaments to membrane glycoproteins, and thus, accounts for the cellular 3D structure (16). Another protein, CD151, expressed highly under the RFB condition, plays an important role both in cell adhesion by binding integrin and in signal transduction to control cell growth (17, 18). Elevated expressions of genes encoding structural proteins in FLCs in the bioreactor might explain the morphological characteristics of such cells. FLC-7 cultured in an RFB had centrally located spheroid nuclei, developed microvillus-like projections, and attached to adjacent cells at localized and specific sites (13). Because these features are characteristic of the

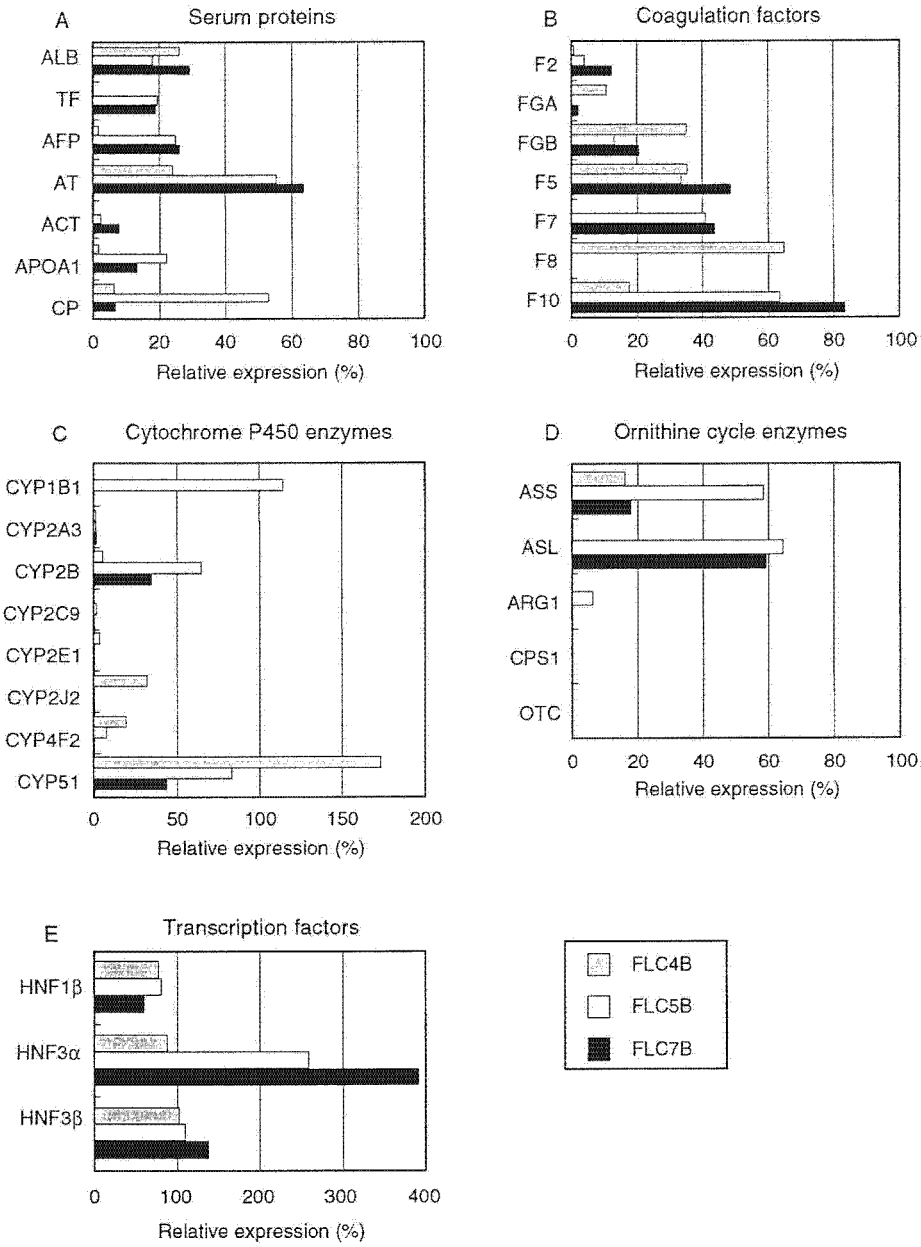

Fig. 3. Comparison of expression levels of genes encoding liver-function-related proteins. The relative expression level of each gene is expressed as a percentage of the counterpart in the normal liver sample, except for α-fetoprotein, where the expression level in HepG2 grown on dishes was used as a reference. Gray bars, FLC-4 in RFB; open bars, FLC-5 in RFB; closed bars, FLC-7 in RFB. ALB, albumin; TF, transferrin; AFP, α-fetoprotein; AT, α1-antitrypsin; ACT, α1-antichymotrypsin; CP, ceruloplasmin; F2, thrombin; FGA, fibrinogen α chain; FGB, fibrinogen β chain; F5, Factor V; F7, Factor VII; F8, Factor VIII; CYP, cytochrome P450; ASS, argininosuccinate synthase; ASL, argininosuccinate lyase; ARG1, arginase I; CPS1, carbamyl phosphate synthetase I; OTC, ornithine transcarbamylase; HNF, hepatocyte nuclear factor.

normal liver cells, higher expression levels of genes encoding structural proteins would indicate that the RFB creates a more physiological environment than that of a monolayer culture. Furthermore, development of intercellular spaces observed in RFB cultures should allow for effective distribution of oxygen and nutrients to cells and facilitate efficient removal of metabolic wastes. Genes that showed significantly

lower expression levels under the RFB culture condition compared with the monolayer condition included the genes for AFP, regulator of G-protein signaling 2 (RGS2), galectin 3 (LGALS3), α1-antitrypsin member 6 (SERPINA6), and phenylalanine hydroxylase (PAH). A higher expression of AFP is related to fetal development and cancer formation, that of RGS2 is related to acute myelogenous and lymphoblastic leukemia (19), and that of LGALS3 gene is related to hepatic and colorectal carcinogenesis (20). Thus, the significantly lower expression of these genes may be related to the undifferentiated state of cells grown in a monolayer culture. Furthermore, the SERPINA6 gene is known to be induced in HepG2 cells by hypoxic conditions (21) and PAH gene expression is correlated with cell density in a culture (22). Based on these results, we speculate that the changes in the gene expression between the RFB and monolayer cultures may reflect the non-physiological condition in the latter.

Each of the three FLCs expressed a subset of the CYP genes. However, evaluation of the drug-metabolizing abilities of FLCs would require more precise studies under different culture conditions or in the presence of pharmacological agents, because it is known that expression of the CYP genes is induced by certain drugs (23, 24). It is known that the expression of CYP and other liver-specific genes is under the transcriptional control of HNFs (25). In particular, the HNF-4 family may play a key role in hepatocyte differentiation (26, 27). Although our GeneChip analysis failed to detect the HNF-4 gene expression in the FLCs in the present study, Northern blot and real-time polymerase chain reaction (PCR) analyses revealed the expression of HNF-4 gene in all the three FLCs under both BAL and monolayer culture conditions (12). The same study showed that the expressions of HNF-4 and its downstream genes were enhanced by some drugs in FLC-5 grown in the RFB (12). Nevertheless, the HNF-4 genes may be potential targets of further forced expression studies for enhancement of the liver-specific function in FLCs

Development of a highly functional liver substitute would require reproduction of culture conditions closely resembling those of the living organ. To achieve this, coculturing hepatocytes with other hepatic sinusoidal cells (endothelial cells or Ito cells) is now under investigation. In addition, optimization of culturing conditions such as medium flow rate and application of culture additives to modify the expression of target genes should be a consideration. The data of the global gene expression analysis may be useful for identifying such target genes or appropriate markers to monitor the improvement of liver-specific function.

Acknowledgements

We profusely thank Drs. Satoru Mizutani and Aruto Yoshida of Kirin Brewery for cluster analysis. We also thank Miyuki Agawa for technical support with the microarray hybridization. This work was supported in part by grants-in-aid from the Promotion and Mutual Aid Corporation for Private School of Japan, University Start-Ups Creation Support System, and from The Japan Health Sciences Foundation (Research on Health Sciences focusing on Drug Innovation, KH71068).

References

1. van de Kerkhove MP, Hoekstra R, Chamuleau RA, van Gulik TM. Clinical application of bioartificial liver support systems. *Ann Surg* 2004; **240**: 216–30.
2. Nagamori S, Hasumura S, Matsuura T, Aizaki H, Kawada M. Developments in bioartificial liver research: concepts, performance, and applications. *J Gastroenterol* 2000; **35**: 493–503.
3. te Velde AA, Ladiges NC, Flendrig LM, Chamuleau RA. Functional activity of isolated pig hepatocytes attached to different extracellular matrix substrates. Implication for application of pig hepatocytes in a bioartificial liver. *J Hepatol* 1995; **23**: 184–92.
4. Morsiani E, Brogli M, Galavotti D, *et al.* Long-term expression of highly differentiated functions by isolated porcine hepatocytes perfused in a radial-flow bioreactor. *Artif Organs* 2001; **25**: 740–8.
5. Rozga J, Podesta L, LePage E, *et al.* Control of cerebral oedema by total hepatectomy and extracorporeal liver support in fulminant hepatic failure. *Lancet* 1993; **342**: 898–9.
6. Neuzil DF, Rozga J, Moscioni AD, *et al.* Use of a novel bioartificial liver in a patient with acute liver insufficiency. *Surgery* 1993; **113**: 340–3.
7. Sussman NL, Finegold MJ, Barish JP, Kelly JH. A case of syncytial giant-cell hepatitis treated with an extracorporeal liver assist device. *Am J Gastroenterol* 1994; **89**: 1077–82.
8. Yamashita Y, Shimada M, Tsujita E, *et al.* Polyurethane form/spheroid culture system using human hepatoblastoma cell line (HepG2) as a possible new hybrid artificial liver. *Cell Transplant* 2001; **10**: 717–22.
9. Takahashi M, Ishikura H, Takahashi C, *et al.* Immunologic considerations in the use of cultured porcine hepatocytes as a hybrid artificial liver. Anti-porcine hepatocyte human serum. *ASAIO J* 1993; **39**: M242–6.
10. van der Laan LJ, Lockey C, Griffeth BC, *et al.* Infection by porcine endogenous retrovirus after islet xenotransplantation in SCID mice. *Nature* 2000; **407**: 90–4.
11. Fujise K, Nagamori S, Hasumura S, *et al.* Integration of hepatitis B virus DNA into cells of six established human hepatocellular carcinoma cell lines. *Hepato Gastroenterol* 1990; **37**: 457–60.
12. Iwahori T, Matsuura T, Maehashi H, *et al.* CYP3A4 inducible model for in vitro analysis of human drug metabolism using a bioartificial liver. *Hepatology* 2003; **37**: 665–73.

13. Kawada M, Nagamori S, Aizaki H, *et al.* Massive culture of human liver cancer cells in a newly developed radial flow bioreactor system: ultrafine structure of functionally enhanced hepatocarcinoma cell lines. *In Vitro Cell Dev Biol* 1998; **34**: 109–15.
14. Aizaki H, Nagamori S, Matsuda M, *et al.* Production and release of infectious hepatitis C virus from human liver cell cultures in the three-dimensional radial-flow bioreactor. *Virology* 2003; **314**: 16–25.
15. Eisen BM, Spellman PT, Brown PO, Botstein D. Cluster analysis and display of genome-wide expression patterns. *Proc Natl Acad Sci USA* 1998; **95**: 14863–8.
16. Gorlin JB, Yamin R, Egan S, *et al.* Human endothelial actin-binding protein (ABP-280, nonmuscle filamin): a molecular leaf spring. *J Cell Biol* 1990; **111**: 1089–105.
17. Hasegawa H, Utsunomiya Y, Kishimoto K, Yanagisawa K, Fujita S. SFA-1, a novel cellular gene induced by human T-cell leukemia virus type 1, is a member of the transmembrane 4 superfamily. *J Virol* 1996; **70**: 3258–263.
18. Zhang XA, Kazarov AR, Yang X, Bontrager AL, Stipp CS, Hemler ME. Function of the tetraspanin CD151-α6β1 integrin complex during cellular morphogenesis. *Mol Biol Cell* 2002; **13**: 1–11.
19. Wu HK, Heng HH, Shi XM, *et al.* Differential expression of a basic helix–loop–helix phosphoprotein gene, G0S8, in acute leukemia and localization to human chromosome 1q31. *Leukemia* 1995; **9**: 1291–8.
20. Nakamura M, Inufusa H, Adachi T, *et al.* Involvement of galectin-3 expression in colorectal cancer progression and metastasis. *Int J Oncol* 1999; **15**: 143–8.
21. Wenger RH, Rolfs A, Marti HH, Bauer C, Gassmann M. Hypoxia, a novel inducer of acute phase gene expression in a human hepatoma cell line. *J Biol Chem* 1995; **270**: 27865–70.
22. McClure D, Miller MR, Shiman R. Cell density dependent regulation of phenylalanine hydroxylase activity in hepatoma cells. Evidence for both an active and inactive enzyme form. *Exp Cell Res* 1976; **98**: 223–36.
23. Tateishi T, Kumai T, Watanabe M, Tanaka M, Kobayashi S. A comparison of the effect of five phenothiazines on hepatic CYP isoenzymes in rats. *Pharmacol Toxicol* 1999; **85**: 252–6.
24. Krusekopf S, Roots I, Hildebrandt AG, Kleeberg U. Time-dependent transcriptional induction of CYP1A1, CYP1A2 and CYP1B1 mRNAs by H^+/K^--ATPase inhibitors and other xenobiotics. *Xenobiotica* 2003; **33**: 107–18.
25. Cereghini S. Liver-enriched transcription factors and hepatocyte differentiation. *FASEB J* 1996; **10**: 267–82.
26. Kuo CJ, Conley PB, Chen L, Sladek FM, Darnell JE Jr, Crabtree GR. A transcriptional hierarchy involved in mammalian cell-type specification. *Nature* 1992; **355**: 457–61.
27. Späth GF, Weiss MC. Hepatocyte nuclear factor 4 provokes expression of epithelial marker genes, acting as a morphogen in dedifferentiated hepatoma cells. *J Cell Biol* 1998; **140**: 935–46.

Available online at www.sciencedirect.com
SCIENCE DIRECT®
ELSEVIER
Journal of the European Ceramic Society 26 (2006) 501–507
www.elsevier.com/locate/jeurceramsoc

Syntheses of calcium-deficient apatite fibres by a homogeneous precipitation method and their characterizations

Mamoru Aizawa[a,*], Hiroko Ueno[b], Kiyoshi Itatani[b], Isao Okada[b]

[a] *Department of Industrial Chemistry, School of Science and Technology, Meiji University, Kanagawa 214-8571, Japan*
[b] *Department of Chemistry, Faculty of Science and Engineering, Sophia University, Chiyoda-ku, Tokyo 102-8554, Japan*

Available online 10 August 2005

Abstract

Calcium-deficient apatite fibres were successfully synthesized by a homogeneous precipitation method using starting solutions with a Ca/P ratio of 1.00–1.67. In the case of the Ca/P ratio of 1.67, the resulting apatite fibre had long-axes of about 60–100 μm and contained 5.2 mass % of carbonate ions. The Ca/P ratio of apatite fibres could be controlled in the range of 1.53–1.68 by changing the Ca/P ratio of the starting solutions from 1.00 to 1.67. The long-axes and the carbonate contents of the resulting calcium-deficient apatite fibres increased with Ca/P ratio of the starting solutions. These apatite fibres were of single crystal and had a preferred orientation in the *c*-axis direction.

Keywords: Powder-chemical preparation; Fibres; Apatite; Biomedical applications; Calcium-deficient hydroxyapatite

1. Introduction

Hydroxyapatite ($Ca_{10}(PO_4)_6(OH)_2$; HAp) has been widely applied as a biomaterial for substituting human hard tissues,[1,2] and as an adsorbent for chromatography.[3] The HAp crystal has two types of crystal planes, bearing different charges: positive on the *a*-planes and negative on the *c*-planes.[3] Thus, novel properties may be produced by controlling the orientation of the crystal planes. Controlled orientation may be achieved by modifying the morphology of HAp crystals. For example, in order to increase the positive charge on the surface of the HAp fibres, one can grow hexagonal-shaped HAp fibres which are oriented along the *c*-axis so that the *a*(*b*)-plane is wider than the *c*-plane. These apatite fibres have specific adsorptions to negatively charged acidic proteins.

The morphological control of HAp crystals has been reported previously by some researchers. For example, Ioku et al.[4] synthesized apatite whiskers with a long-axis of several micrometers in length by a hydrothermal process and demonstrated by transmission electron microscopy (TEM) that the whiskers were of single crystal. On the other hand, Yokogawa et al.[5] synthesized the plate-shaped apatites by a hydrothermal process in the presence of organic solvents.

We have also successfully synthesized apatite fibres with long axes of 60–100 μm by homogeneous precipitation method.[6,7] It was confirmed from the results of high-resolution transmission electron microscopy (HR-TEM) using a shadow imaging technique that the apatite fibres were of single crystals with the *c*-axis orientation parallel to the long axis of the fibre.[8,9]

Using the above fibres, we have promoted the development of (i) porous HAp ceramics with well-controlled pore sizes[7,10] and (ii) HAp/polymer hybrids possessing mechanical properties similar to those of living cortical bone by in situ bulk polymerization of the monomer in the pores of the ceramic.[11] This hybrid, with mechanical properties similar to those of cortical bone, has been shown to have excellent biocompatibility both in vitro and in vivo.[12,13] In addition, we have developed a three-dimensional scaffold with large interconnected pores of 100–250 μm in diameter and high porosities of 98–99% for tissue engineering of bone from the above-mentioned apatite fibres.[14–16] We have already clarified that the apatite-fibre scaffold has an excellent cellular response, such as enhanced differentiation to osteoblasts.

* Corresponding author. Tel.: +81 44 934 7237; fax: +81 44 934 7906.
E-mail address: mamorua@isc.meiji.ac.jp (M. Aizawa).

0955-2219/$ – see front matter © 2005 Elsevier Ltd. All rights reserved.
doi:10.1016/j.jeurceramsoc.2005.07.007

On the other hands, the constituent ions of HAp crystals can be replaced by many other kinds of ions while maintaining the skeleton, leading to form various substituted apatite compounds.[17] Calcium-deficient hydroxyapatite (Ca-def HAp), $Ca_{10-x}(HPO_4)_x(PO_4)_{6-x}(OH)_{2-x}{\cdot}nH_2O$, belongs to the apatite family.[18] It is well-known that Ca-def HAp has higher chemical activity than pure HAp and forms biodegradable tricalcium phosphate ($Ca_3(PO_4)_2$; TCP)[19] or TCP/HAp biphase by thermal decomposition. Thus, Ca-def HAp may be expected as a starting material to prepare biodegradable bioceramics.

If one can control the Ca/P ratio of the above-mentioned apatite fibres, the fibre-derived bioceramics may have a well-controlled chemical composition. For example, Ca-def HAp fibre with a Ca/P ratio of 1.50 will produce the TCP phase after heat treatment. The aims of the present investigation were to synthesize Ca-def HAp fibres with the controlled Ca/P ratios and to examine some properties, including particle morphology and thermal stability, of the resulting fibres using some suitable techniques.

2. Experimental

2.1. Syntheses of calcium-deficient apatite fibres

Ca-def HAp fibres were synthesized by partly modifying the apatite-fibre processing previously reported.[7] Ten kinds of starting solutions with the Ca/P ratios of 1.00–1.67 were prepared by mixing the 0.100–0.167 mol dm^{-3} $Ca(NO_3)_2$, 0.100 mol dm^{-3} $(NH_4)_2HPO_4$, 0.500 mol dm^{-3} $(NH_2)_2CO$ and 0.10 mol dm^{-3} HNO_3 aqueous solutions. Concentrations of Ca^{2+} ion in the starting solution were 0.100, 0.110, 0.120, 0.130, 0.140, 0.150, 0.155, 0.160, 0.164 and 0.167 mol dm^{-3}.

Each starting solution (0.5 dm^3) was refluxed at 80 °C for 24 h to form octacalcium phosphate ($Ca_8H_2(PO_4)_6{\cdot}5H_2O$; OCP) via $CaHPO_4$ and then the resulting OCP was converted into HAp by refluxing at 90 °C for 72 h. The pH in the solution increased from ~3 to ~8, owing to the NH_3 formed by the hydrolysis of the urea as a precipitating agent. The products were composed of fibre-shaped particles and granules. The fibre fractions were easily separated by decantation; the yield of the fibre was in range of 50–60%.

2.2. Characterization of the resulting calcium-deficient apatite fibres

The crystalline phases of the powders were identified using an X-ray powder diffractometer (XRD; RINT2000PC, Rigaku; 40 kV, 40 mA). The lattice constants were calculated by the least-squares method using the JADE program attached to RINT2000PC. Fourier transform infrared spectroscopy (FT-IR) was performed using Shimadzu 8200, the measuring range of which was 400–4000 cm^{-1}.

The contents of calcium and phosphorus in each fibre were determined using an inductively coupled plasma emission spectrometer (ICP-ES; Seiko, SPS-7700). The contents of carbon in the fibre were measured using an element analyzer (PE2400-II, Perkin–Elmer).

The morphologies were observed using a scanning electron microscope (SEM; Hitachi, S-4500) and a TEM (JEOL, CX200). TEM samples were prepared by dispersing the fibres in ethanol and collecting them onto Cu mesh TEM grids.

2.3. Thermal stability of the resulting calcium-deficient apatite fibres

The differential thermal analysis and thermogravimetry (DTA-TG; Rigaku, Thermo Plus TG8120) were carried out using about 15 mg of the fibre at a heating rate of 10 °C min^{-1}. In addition, we performed XRD measurement of the fibre heated at 1200 °C for 1 h.

3. Results and discussion

3.1. Syntheses of calcium-deficient apatite fibres and their characterizations

Fig. 1 shows the XRD patterns for the products from typical starting solutions with various Ca/P ratios. In the case of the Ca/P = 1.67 of the starting solution (Fig. 1(a)), the HAp was present in the sample powder, and the (1 0 0), (2 0 0) and (300) reflections of the resulting apatite were more intense than those of the typical HAp listed in JCPDS card #9–432. The XRD pattern changed to the typical HAp pat-

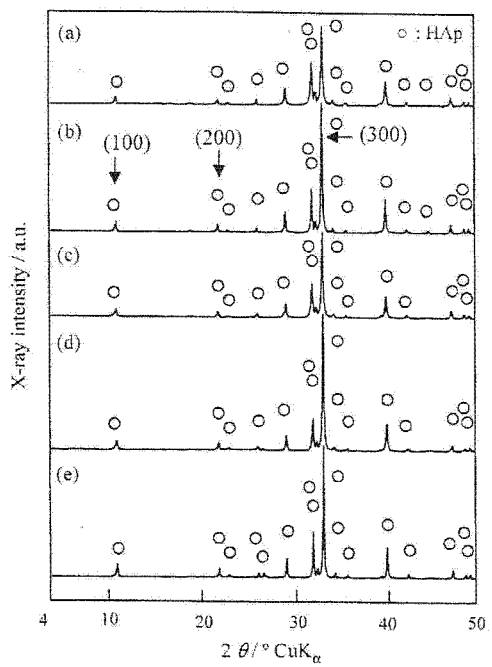

Fig. 1. XRD patterns of the products from typical starting solutions with various Ca/P ratios. (a) Ca/P ratio of 1.67, (b) 1.60, (c) 1.40, (d) 1.20 and (e) 1.00.

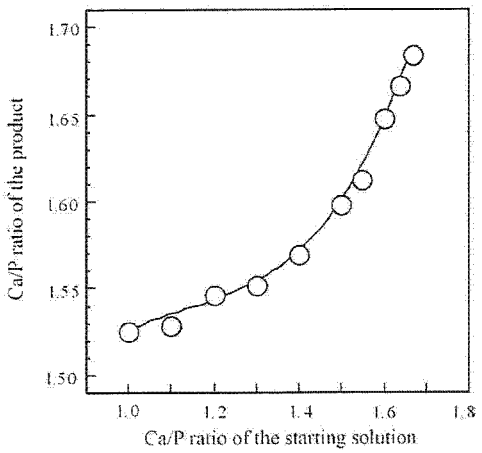

Fig. 2. Relationship between Ca/P ratio of the product and nominal Ca/P ratio of the starting solution.

tern after crushing the sample using a mortar and a pestle. In the cases of Fig. 1 (b)–(e), the products consisted of uniform apatite phase and had the XRD reflections characteristic of the (1 0 0), (2 0 0) and (3 0 0) planes. These results indicate that the present apatite gives preferred orientation in the *c*-axis direction of the hexagonal crystal, leading to develop the *a*- or *b*-plane of the apatite crystal.

The Ca/P molar ratios of the above-mentioned apatite were determined using an ICP-ES. Fig. 2 shows the relationship between Ca/P ratio of the product and nominal Ca/P ratio of the starting solution. The Ca/P ratio of the product increased with nominal Ca/P ratio of the starting solution. This result shows that the Ca/P ratio of the product can be easily controlled in the range of 1.53–1.69 by changing the Ca/P ratio of the starting solutions from 1.00–1.67.

Fig. 3 shows the FT-IR spectra of the resulting apatite with well-controlled Ca/P ratio. In the case of the Ca/P = 1.67 of the starting solution (Fig. 3(a)), the absorptions at 1300–900, 600 and 570 cm^{-1} assignable to the PO_4^{3-} groups and those at 3570 and 630 cm^{-1} assigned to the OH^- group were detected. In addition, the absorptions assignable to the CO_3^{2-} group were detected at 1600–1400 and ~880 cm^{-1} in the present investigation, as shown by the arrow marks.

As for the incorporation of CO_3^{2-} into HAp, Monma and Takahashi[20] reported as follows: (i) when the CO_3^{2-} group substitutes for the PO_4^{3-} group in the HAp (Type B of cabonate-containing HAp (CO_3HAp)), the characteristic absorptions appear at 1455, 1430, 1415 and 872 or 862 cm^{-1}; (ii) when the CO_3^{2-} group substitutes for the OH^- group in the HAp (Type A of the CO_3HAp), the absorptions appear at 1542 or 1546, 1465 and 879 or 883 cm^{-1}. As shown in Fig. 3, the present absorptions indicate that the CO_3^{2-} group substitutes for both PO_4^{3-} and OH^- groups in the HAp structure. Thus the present HAp powder can be referred to as Type AB of CO_3HAp. The formation of this CO_3HAp may be due to the generation of CO_2 through the hydrolysis of the $(NH_2)_2CO$.

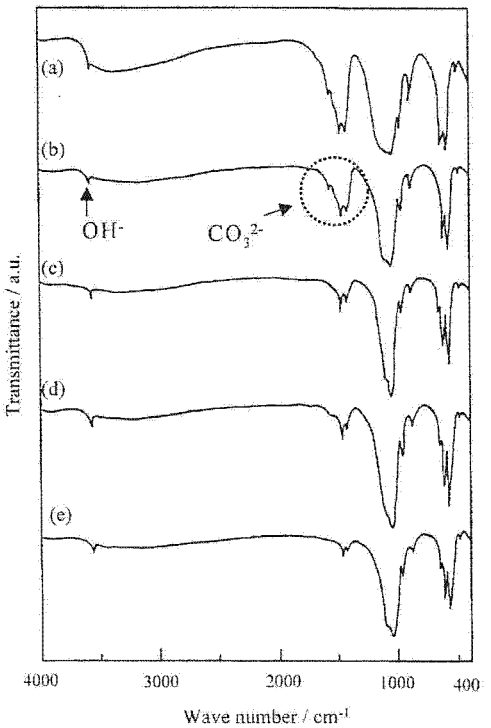

Fig. 3. FT-IR spectra of the resulting Ca-def HAp from typical starting solutions with various Ca/P ratios. (a) Ca/P ratio of 1.67, (b) 1.60, (c) 1.40, (d) 1.20 and (e) 1.00.

In the cases of Fig. 3(b)–(e), the FT-IR spectra of the resulting apatite with the lower Ca/P ratio of 1.67 are assignable to those of the typical CO_3HAp. However, the absorption assigned to the CO_3^{2-} group decreased with increasing Ca/P ratio of the resulting apatite. Thus, we performed elemental analysis of the resulting apatite in order to determine the actual carbon content. The result is shown in Fig. 4.

The figure illustrates the relationship between CO_3^{2-} content of the resulting apatite and Ca/P ratio of the product. The

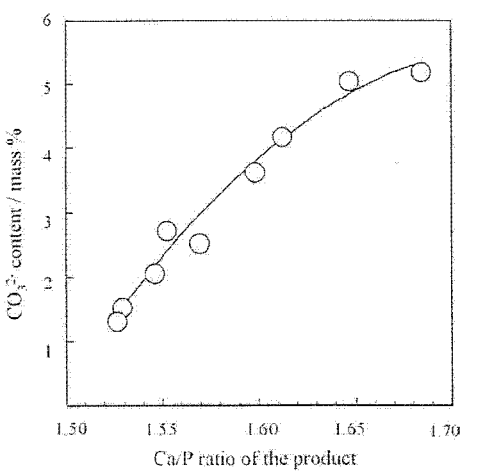

Fig. 4. Relationship between CO_3^{2-} content and Ca/P ratio of the Ca-def HAp.

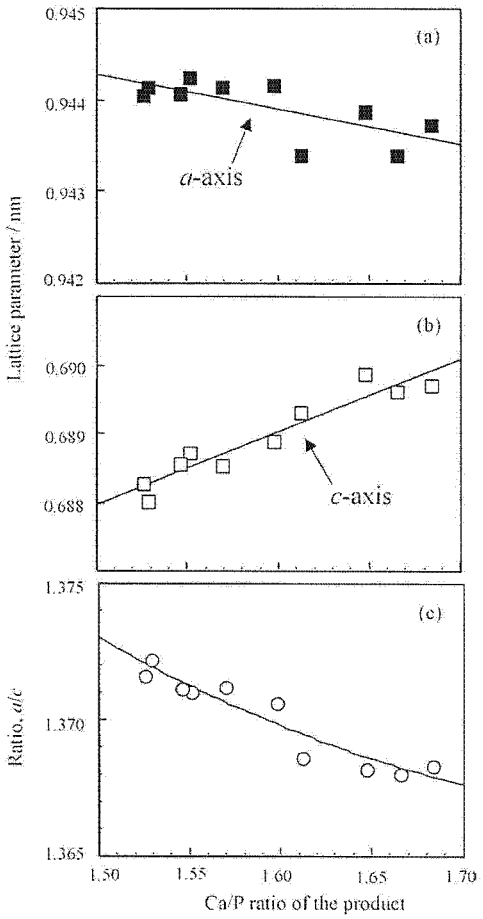

Fig. 5. Lattice parameters of the *a*-axis (a) and *c*-axis (b) and the *a*/*c* ratio (c) against the Ca/P ratio of the Ca-def HAp.

CO_3^{2-} content of the resulting apatite increased from ~1 to ~5 mass% with the Ca/P ratio of the product. Both results of FT-IR and elemental analysis show that the incorporation of CO_3^{2-} into apatite structure is depressed by decreasing the Ca/P ratio of the starting solution.

The above-mentioned phenomena suggest that, when the Ca/P ratio of the starting solution is less than 1.67, HPO_4^{2-} will be incorporated into the PO_4^{3-} site of the apatite structure to compensate the charge imbalance caused by the lack of Ca^{2+} ions. Although many CO_3^{2-} ions are also incorporated into the PO_4^{3-} site of the HAp structure, the HPO_4^{2-} ions will be easier to incorporate into HAp structure than the CO_3^{2-} ions in the experimental conditions if one takes the solubility products of $CaCO_3$ and HAp into account. Thus, the CO_3^{2-} contents in the Ca-def HAp may decrease with decreasing Ca/P ratio of the starting solution.

Next, we measured the lattice parameters of the *a*-axis and the *c*-axis. The results are shown in Fig. 5(a) and (b), together with the *a*/*c* ratio (Fig. 5(c)). With increasing Ca/P ratio of the resulting apatite, the lattice parameter of the *a*-axis slightly decreased, while that of the *c*-axis increased. In addition, the *a*/*c* ratio decreased with increasing Ca/P ratio of the resulting apatite.

According to Elliott,[21] the lattice parameters of crystalline Ca-def HAp increase in the *a*-axis direction with decreasing Ca/P ratio, but decrease in the *c*-axis direction. Thus, the *a*/*c* ratio increases with a decrease in the Ca/P ratio. The present result is consistent with the above findings. The increase in the *a*-axis parameter with decreasing Ca/P ratio may be due to more incorporation of HPO_4^{2-} ion into Ca-def HAp structure.

3.2. Morphologies of the resulting calcium-deficient apatite fibres

Fig. 6 shows that SEM micrographs of the apatite synthesized from starting solutions with the Ca/P ratios of 1.00 (Fig. 6(a)), 1.40 (Fig. 6(b)) and 1.67 (Fig. 6(c)). It can be seen from these SEM observations that the resulting apatites are composed of fibre-shaped particles with long-axes of ~60 to ~100 μm. All the synthesized apatites had morphologies of such fibre shape. In addition, the short-axis size of the fibre slightly decreased with increasing Ca/P ratio. This result indicates that the aspect ratio of the fibres increases with the Ca/P ratio. Judging from these observations and the XRD results, we consider that these Ca-def HAp fibres may elongate along the direction of the *c*-axis to develop the *a*- and *b*-planes of the hexagonal crystals.

Fig. 7 shows the TEM micrograph of the typical Ca-def HAp fibres, together with the selected area electron diffraction (SAED). SAED observations were performed in four areas (A, B, C and D) along the long-axis of the fibre. The

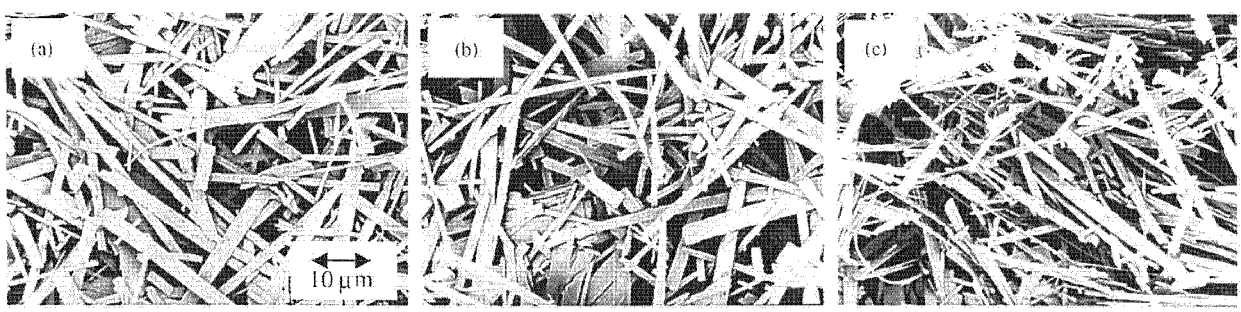

Fig. 6. SEM micrographs of the Ca-def HAp fibres synthesized from starting solutions with the Ca/P ratios of 1.00 (a), 1.40 (b) and 1.67 (c).

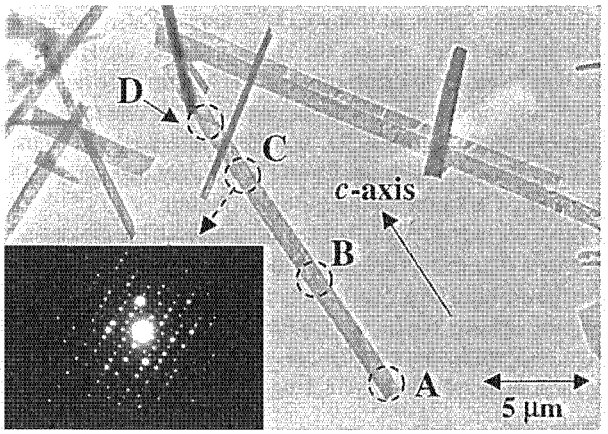

Fig. 7. TEM micrograph of typical Ca-def HAp fibres, together with the SAED pattern from area C. Synthesis conditions; (i) starting solution: Ca/P ratio of 1.50, (ii) heating temperature and time: 80 °C for 24 h and then 90 °C for 72 h.

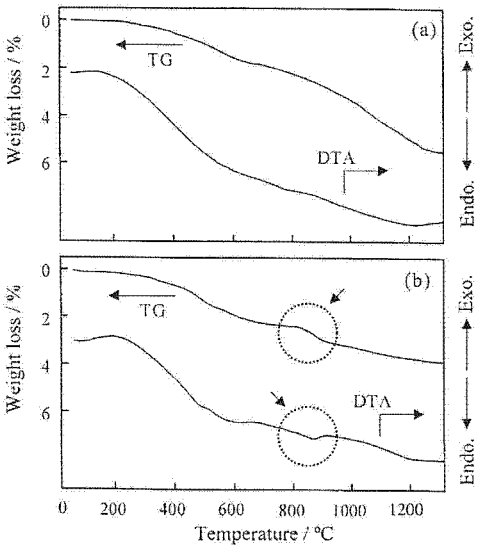

Fig. 9. DTA-TG curves of the Ca-def HAp fibres synthesized from the starting solutions with Ca/P ratios of 1.60 (a) and 1.00 (b).

diffraction pattern from area C showed distinct spots corresponding to an apatite structure with high crystallinity. The other diffraction patterns had similar geometry to the pattern in the area C. As all diffraction patterns showed the same geometry along the long-axis of the fibre, it was concluded that the present Ca-def HAp fibres were of single crystal.

The microstructure of the single-crystal Ca-def HAp fibres was examined on the basis of both bright and dark field images. The results are shown in Fig. 8. The bright field image (Fig. 8(a)) illustrates black contours oriented across the short axis of the fibre. In addition to the black contours, many ripples were also observed in the fibres. The contrast from these contours was also observed in dark field image (Fig. 8(b)). Tilting experiments confirmed that this contrast arose due to strain in the fibres, i.e. that they are bend contours and not defects. Our TEM observations illustrate that the fibres are highly strained single crystals.

We conclude that the present single-crystal Ca-def HAp fibres preferentially grow along the *c*-axis to develop the *a*(*b*)-plane of the hexagonal HAp.

3.3. Thermal stability of the resulting calcium-deficient apatite fibres

The phase changes of the Ca-def HAp during heating were examined using DTA-TG and XRD. Fig. 9 shows the DTA-TG curves of the Ca-def HAp fibres synthesized from the starting solutions with the Ca/P ratios of 1.60 (Fig. 9(a)) and 1.00 (Fig. 9(b)). The actual Ca/P ratios of the prepared Ca-def HAp fibres were 1.65 and 1.53, respectively. In Fig. 9(a), the TG curve demonstrates a continuous weight loss above 200 °C, while the DTA curve shows an endothermic

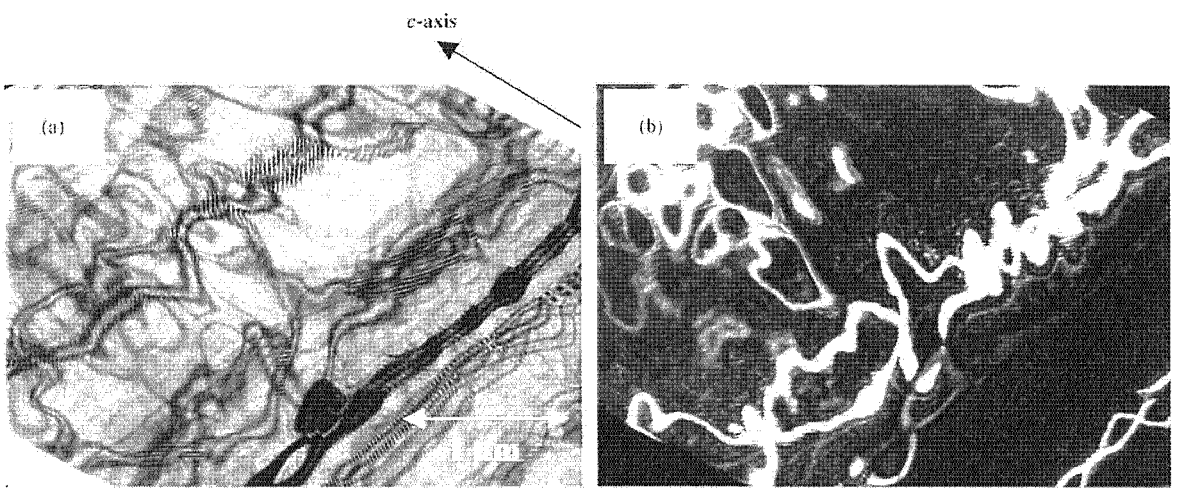

Fig. 8. TEM micrographs of the Ca-def HAp fibres synthesized from starting solutions with the Ca/P ratio of 1.50. (a) Bright- and (b) dark-field imaging.

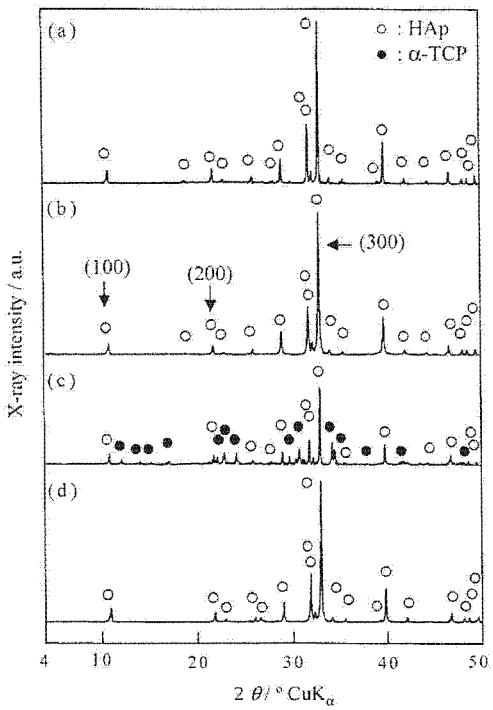

Fig. 10. XRD pattern of the Ca-def HAp fibres before (b, d) and after heat treatment at 1200 °C for 1 h (a, c); (a, b) Ca-def HAp fibres synthesized from the starting solution with the Ca/P ratio of 1.60 and (c, d) the Ca/P ratio of 1.00.

change over the measured temperature range. This apparent endothermic change may be due only to the drift of the base line.

In the case of Fig. 9 (b), the TG curve shows the weight loss in the range of 800–1000 °C, as pointed by the arrow mark. The DTA curve also shows an endothermic reaction in the range of 800–1000 °C, corresponding to the weight loss of the TG curve. These weight loss and endothermic reaction may be due to the decomposition of the Ca-def HAp into the TCP.

Fig. 10 shows the XRD pattern of the Ca-def HAp fibres before (Fig. 10(b and d)) and after heat treatment at 1200 °C for 1 h (Fig. 10(a and c)). These testing samples correspond to those of the DTA-TG measurement. Fig. 10(a) and (b) show the XRD patterns of the Ca-def HAp fibres synthesized from the starting solution with the Ca/P ratio of 1.60. These XRD patterns show that the testing samples consisted of apatite single phase, which has preferred orientation in the *c*-axis direction, and that no changes occurred in the crystalline phase during heat treatment. On the other hand, in the case of Fig. 10(c) and (d), the single apatite phase was present in the sample before the heat treatment, while the HAp/TCP biphase present in the heated sample. These results indicate that the present Ca-def HAp fibre technology will be effective for creating the biodegradable materials consisting of TCP phase or TCP/HAp biphase.

4. Conclusions

Calcium-deficient apatite (Ca-def HAp) fibres were successfully synthesized by a homogeneous precipitation method using starting solutions with Ca/P ratio of 1.00–1.67. In the case of the Ca/P ratio of 1.67, the resulting apatite fibre had long-axes of about 60–100 μm and contained 5.2 mass% of carbonate ions. The Ca/P ratio of the apatite fibres could be controlled in the range of 1.53–1.68 by changing the Ca/P ratio of the starting solutions from 1.00 to 1.67. The long-axes and the carbonate contents of the resulting calcium-deficient apatite fibres increased with the Ca/P ratio of the starting solutions. These apatite fibres were of single crystal and had a preferred orientation in the *c*-axis direction. The resulting Ca-def HAp fibres were decomposed to form the HAp/TCP biphase. The present technology will be effective for creating the biodegradable materials consisting of TCP phase or TCP/HAp biphase.

References

1. Hench, L. L., Bioceramics. *J. Am. Ceram. Soc.*, 1998, **81**, 1705–1728.
2. Hench, L. L., Bioceramics: For concept to clinic. *J. Am. Ceram. Soc.*, 1991, **74**, 1487–1510.
3. Kawasaki, T., Hydroxyapatite as a liquid chromatographic packing. *J. Chromatogr.*, 1991, **544**, 147–184.
4. Ioku, K., Yoshimura, M. and Somiya, S., Hydrothermal synthesis of ultrafine hydroxyapatite single crystals. *Nihon-Kagaku-Kaishi*, 1988, **1988**, 1565–1570.
5. Nagata, F., Yokogawa, Y., Toriyama, M., Kawamoto, Y., Suzuki, T. and Nishizawa, K., Hydrothermal synthesis of hydroxyapatite crystals in the presence of methanol. *J. Ceram. Soc. Jpn.*, 1995, **103**, 70–73.
6. Aizawa, M., Kinoshita, M., Yamada, K., Itatani, K. and Kishioka, A., Effects of synthesis and morphology of carbonate-containing hydroxyapatite prepared by homogeneous precipitation method. *Inorg. Mater.*, 1998, **5**, 387–397.
7. Aizawa, M., Howell, F. S., Itatani, K., Yokogawa, Y., Nishizawa, K., Toriyama, M. *et al.*, Fabrication of porous ceramics with well-controlled open pores by sintering of fibrous hydroxyapatite particles. *J. Ceram. Soc. Jpn.*, 2000, **108**, 249–253.
8. Aizawa, M., Porter, A. E., Best, S. M. and Bonfield, W., High resolution transmission electron microscopy investigation of single crystal apatite fibres synthesized by a homogeneous precipitation method. *Key Eng. Mater.*, 2003, **240–242**, 509–512.
9. Aizawa, M., Porter, A. E., Best, S. M. and Bonfield, W., Microstructual changes of single-crystal apatite fibres during heat treatment. *Key Eng. Mater.*, 2004, **254–256**, 915–918.
10. Kawata, M., Uchida, H., Itatani, K., Okada, I., Koda, S. and Aizawa, M., Development of porous ceramics with well-controlled porosities and pore sizes from apatite fibers and their evaluations. *J. Mater. Sci. Mater. Med.*, 2004, **15**, 817–823.
11. Aizawa, M., Tsuchiya, Y., Itatani, K., Suemasu, H., Nozue, A. and Okada, I., Fabrication of hybrid materials by the introduction of poly(methylmethacrylate) into the porous hydroxyapatite ceramics. *Bioceramics*, 1999, **12**, 453–456.
12. Aizawa, M., Ito, M., Itatani, K., Suemasu, H., Nozue, A., Okada, I. *et al.*, In vivo and in vitro evaluation of the biocompatibility of the hydroxyapatite-PMMA hybrid materials having mechanical property similar to that of cortical bone. *Key Eng. Mater.*, 2001, **218–220**, 465–468.

13. Aizawa, M., Ito, M., Itatani, K., Okada, I. and Matsumoto, M., Development of bioactive tailor-made materials by inorganic/organic hybridization. *Phosphor. Lett.*, 2003, **46**, 7–14.
14. Aizawa, M., Ueno, H., Itatani, K. and Okada, I., Development of scaffolds for tissue engineering using single-crystal apatite fibres and their biological evaluation by osteoblastic cell. *Trans. Mater. Res. Soc. Jpn.*, 2003, **28**, 849–852.
15. Aizawa, M., Shinoda, H., Uchida, H., Itatani, K., Okada, I., Matsumoto, M. *et al.*, Development and biological evaluation of apatite fiber scaffolds with large pore size and high porosity for bone regeneration. *Key Eng. Mater.*, 2003, **240–242**, 647–650.
16. Aizawa, M., *Culture Method of Osteoblast*, Japan patent Tokukai 2003-93052, 2 April, 2003.
17. Kreidler, E. R. and Hummel, F. A., The crystal chemistry of apatite: structure fields of fluor- and chloroapatite. *Am. Mineral.*, 1970, **55**, 170–184.
18. Monma, H., Ueno, S. and Kanazawa, T., Properties of hydroxyapatite prepared by the hydrolysis of tricalcium phosphate. *J. Chem. Tech. Biotechnol.*, 1981, **31**, 15–24.
19. Irie, H., Bone substitute to be remodeled to natural bone. *Bull. Ceram. Soc. Jpn.*, 2003, **38**, 55–57.
20. Monma, H. and Takahashi, T., Preparation and thermal changes of carbonate-containing apatite. *Gypsum Lime*, 1987, **210**, 287–291.
21. Elliott, J. C., *Structure and Chemistry of the Apatites and other Calcium Orthophosphates*. Amsterdam-London-New York-Tokyo, Elsevier, 1994, pp. 151–52.

Syntheses of silicon-containing apatite fibres by a homogeneous precipitation method and their characterization

Mamoru Aizawa[1,a], Nelesh Patel[2,b], Alexandra E. Porter[2,c], Serena M. Best[2,d] and William Bonfield[2,e]

[1]Department of Industrial Chemistry, School of Science and Technology, Meiji University, 1-1-1 Higashimita, Tama-ku, Kawasaki, Japan, 214-8571

[2]The Cambridge Centre for Medical Materials, Department of Materials Science and Metallurgy, University of Cambridge, Pembroke Street, Cambridge, CB2 3QZ, UK

[a]mamorua@isc.meiji.ac.jp, [b]ez8046@yahoo.co.uk, [c]aep30@cam.ac.uk, [d]smb51@cam.ac.uk, [e]wb210@cam.ac.uk

Keywords: Hydroxyapatite, Apatite fibre, Silicon-containing apatite, Homogeneous precipitation method

Abstract. Silicon-containing apatite (Si-HAp) fibres were successfully synthesized by a homogeneous precipitation method. The resulting Si-HAp fibres were composed of carbonate-containing apatite fibres with preferred orientation along the (h00) planes. The Si contents in the Si-HAp fibres could be controlled by the Si concentration of the starting solutions. TEM observation indicated that the Si-HAp fibres were single crystals. The Si-HAp fibres have potential as novel materials for high-performance biomedical devices.

Introduction

Hydroxyapatite ($Ca_{10}(PO_4)_6(OH)_2$; HAp) is used in biomedical applications, such as bone grafts and scaffolds for bone tissue engineering [1]. The composition of synthetic HAp is a similar to bone mineral; however, there are a number of distinct differences between the two materials in terms of their trace ion contents. In recent investigations, the bioactivity of the HAp has been shown to be enhanced by the substitution of suitable ions into its crystal lattice. For example, substitution of low levels of silicon into the HAp lattice has been found to dramatically improve the rate at which bone bonding occurs with the implant materials [2, 3].

HAp crystals belong to a hexagonal crystal system and possess a positive charge in their *a*-planes and the negative charge in their *c*-planes [4]. If one can control the morphology of the HAp crystal, the products can be applied as novel materials for biomedical devices using surface charges [1]. The authors have reported that apatite fibres can be synthesized by a homogeneous precipitation method (HPM) [5], and that the fibre was single-crystal and highly strained [6].

Our aims in the present investigation are to create novel high-performance apatite fibres with a trace level of silicon and to examine some properties of the resulting fibres.

Experimental

The silicon-containing apatite (Si-HAp) fibres were synthesized as follows, based on modification of methods reported previously [5, 6]. Starting solutions were prepared using calcium salts ($Ca(NO_3)_2 \cdot 4H_2O$), phosphates ($(NH_4)_2HPO_4$), silicates ($Si(OC_2H_5)_4$; TEOS), urea ($(NH_2)_2CO$) and nitric acid (HNO_3). The concentrations of Ca^{2+}, PO_4^{3-} and SiO_4^{4-} ions in the starting solution were 0.167 mol•dm^{-3} and 0.0861 to 0.100 mol•dm^{-3}, and 0 to 13.9 x 10^{-3} mol•dm^{-3}, respectively; the Ca/(P+Si) molar ratio was fixed at 1.67. The concentration of urea was 0.50 mol•dm^{-3}. For example, in the case of the addition of Si 0.8 mass% in the Si-HAp fibres as a nominal composition, the concentrations in the starting solution were 0.167 mol•dm^{-3} Ca^{2+} ions, 0.09547 mol•dm^{-3} PO_4^{3-} ions, 4.57 x 10^{-3} mol•dm^{-3} SiO_4^{4-} ions and 0.50 mol•dm^{-3} urea.

The precursor phase for the Si-HAp fibres, octacalcium phosphate ($Ca_8H_2(PO_4)_6 \cdot 5H_2O$; OCP) fibres, was first prepared by heating the above starting solution at 80°C for 24 h. The resulting OCP fibres were transformed into Si-HAp fibres by heating at 95°C for 144 h in the presence of the TEOS. The urea in the starting solution played the role of controlling the pH in the reaction system. The products had two morphologies: fibres and granules. These could be easily separated by a decantation.

The resulting Si-HAp fibres were characterized by various techniques including X-ray diffractometry (XRD), Infrared spectrophotometry (IR), scanning electron microscopy (SEM), energy dispersion X-ray analysis (EDX), X-ray fluorescence (XRF) and transmission electron microscopy (TEM). In addition, we heated the fibres at 1200℃ for 1 h to examine the phase changes by XRD, in order to assess the thermal stability of the Si-HAp.

Results and discussion

Single HAp phase was present in all the fibre- and granular-shaped products. Figure 1 shows typical XRD patterns of the resulting apatite with 0.8 mass% of Si as a nominal composition: (a) fibres and granular (b). The (100), (200) and (300) reflections of the apatite fibres were more intense than those of a typical HAp listed in JCPDS card #9-432 (Fig. 1(a)); however, the XRD pattern of crushed fibres was more similar to that of typical HAp. The HAp was also present in the granules and it showed typical apatite pattern (Fig. 1(c)).

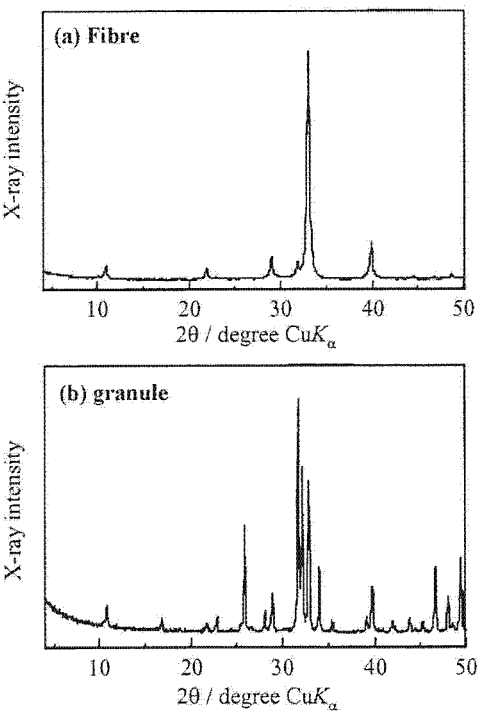

Fig. 1 Typical XRD patterns of the Si-containing apatite: (a) fiber, (b) granule (starting solution: Si 0.8 mass%, heating conditions: 80°C, 24 h, and then 95°C, 144 h).

In the FT-IR spectra of the fibres, the absorptions assigned to the PO_4^{3-} groups at 1300-900, 600 and 570 cm^{-1} and those assigned to the OH^- group at 3570 and 630 cm^{-1} were detected. In addition, the absorptions assigned to CO_3^{2-} were detected at 1600-1400 and ~880 cm^{-1}. The present absorptions indicate that the CO_3^{2-} group substitutes for both PO_4^{3-} and OH^- groups in the HAp structure. Thus, we consider that the resulting Si-HAp fibres were composed of carbonate-containing apatite fibres with preferred orientation along the (h00) planes.

Figure 2 shows typical SEM micrographs of the resulting fibres and granules. In Fig. 2(a), the apatite fibres were ~60 - ~100 μm along the long axis. Judging from this observations and XRD results, we consider that these HAp particles may elongate along the direction of the *c*-axis to develop the *a*- or *b*-plane of the hexagonal crystals. The granules (Fig. 2(b)) were mainly composed of agglomerates of particles with hexagonal cross section.

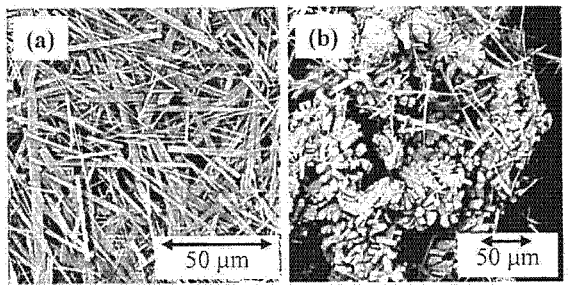

Fig. 2 SEM micrographs of the Si-containing apatite: (a) fiber, (b) granule (starting solution: Si 0.8 mass%, heating conditions: 80°C, 24 h, and then 95°C, 144 h).

According to the EDX spectra of apatite fibres and granular apatite, we noticed that the apatite fibres contained silicon, in spite of absence of silicon in the case of apatite granular. The incorporation of silicon into the fibres will be related with the transform of OCP fibres to HAp fibres in the co-presence of silicate ions.

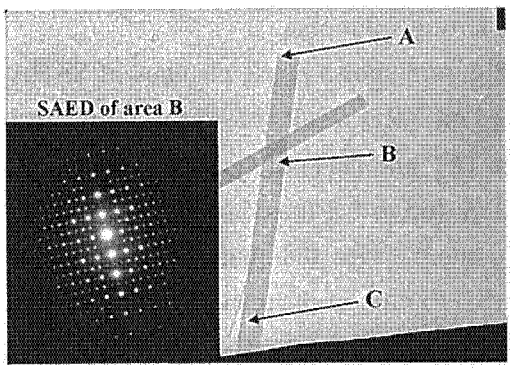

Fig. 3 TEM micrograph of the Si-containing apatite fibre, together with typical SAED pattern of area B (starting solution: Si 0.8 mass%, heating conditions: 80°C, 24 h, and then 95°C, 144 h).

Figure 3 shows typical a TEM micrograph and a selected area electron diffraction image (SAED) of area B. The SAED patterns from point of A, B and C showed clear spots corresponding to an apatite structure with high crystallinity. Three diffraction patterns showed the same geometry along to long-axis of the fibre, it was concluded that the apatite fibres were not polycrystalline, but single crystal. Thus, the TEM observations combined with the XRD and SEM

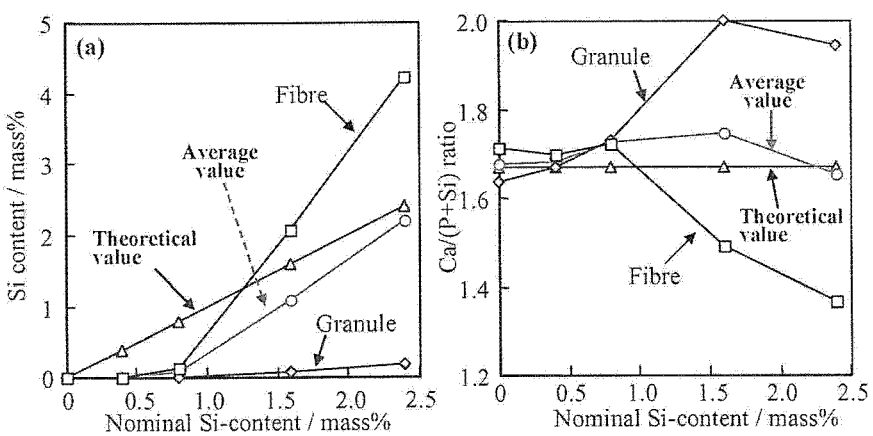

Fig. 4 XRF results of Si-containing apatite: (a) Si content and (b) Ca/(Si+P) molar ratio in the fibre and granule.

results suggested that single crystal apatite fibres may grow along the *c*-axis to develop the *a*(*b*)-plane of hexagonal HAp.

Figure 4(a) shows the Si content in the Si-HAp fibres/granules. The silicon contents in Si-HAp fibres increased with the Si concentration of stating solution. Although the more silicon was incorporated into fibres, little silicon was detected in the granular apatites. Figure 4(b) shows the Ca/(Si+P) ratios of Si-HAp fibres/granules with various Si contents. In the case of Ca/(Si+P) ratio, up to Si=0.8 mass%, the Ca/(Si+P) ratios in fibres and granules were similar to those of the nominal composition in the starting solution. However, in the case of Si=1.6 mass% and 2.4 mass%, the Ca/(Si+P) ratio of fibres decreased less, while that of the granules increased more, compared with Ca/(Si+P) ratio (1.67) nominal composition. These results indicate that the Si contents in Si-HAp fibres could be controlled by the Si conce ntration of the starting solutions.

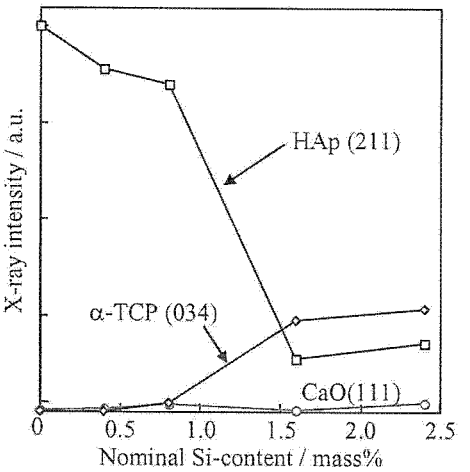

Fig. 5 Phase changes of the Si-containing apatite fibres after heating at 1200°C for 1 h.

Figure 5 shows phase changes of Si-HAp fibres after heating at 1200°C for 1 h. This result is based on XRD results of crushed fibres using three kinds of reflection peaks: (211) of HAp, (034) of α-TCP and (111) of CaO. The HAp phase was still present in the Si-HAp fibres with lower Si content (up to 0.8 mass%), although the α-TCP was formed in the case of the Si-HAp with higher Si content (over 0.8 mass%). This formation of α-TCP may be due to the decrease of the Ca/(Si+P) ratio of the resulting Si-HAp fibres.

Conclusions

The above results indicate that the single-crystal apatite fibres with controlled Si-content were easily synthesized by changing the Si-contents of the starting solutions via the HPM. The Si-HAp fibres have potential as novel materials for high-performance biomedical devices.

Reference

[1] M. Aizawa, H. Shinoda, H. Uchida, I. Okada, T. J. Fujimi, N. Kanzawa, H. Morisue, M. Matsumoto and Y. Toyama: Phosphorus Res. Bull. Vol. 17(2004), p. 268.

[2] I. R. Gibson, J. Huang, S. M. Best and . Bonfield: Bioceramics Vol. 12 (1999), p. 191.

[3] A. E. Porter, S. M. Best and W. Bonfield: J. Biomed. Mater. Res. Vol. 68A (2004), p.133.

[4] T. Kawasaki: J. Chromatogr. Vol. 544 (1991), p. 147.

[5] M. Aizawa, F. S. Howell, K. Itatani, Y. Yokogawa, K. Nishizawa, M. Toriyama and T. Kameyama: J. Ceram. Soc. Jpn. Vol. 108, (2000), p249.

[6] M. Aizawa, A. E. Porter, S. M. Best and W. Bonfield: Biomaterials, Vol. 26, (2004), p. 3427.

DEVELOPMENT OF APATITE-FIBER SCAFFOLDS PROMOTOING HARD-TISSUE REGENERATION AND THEIR APPLICATION TO BIOMEDICAL DEVICES

Mamoru Aizawa[1], Hiroshi Uchida[2], Takahiko J. Fujimi[2], Nobuyuki Kanzawa[2], Morio Matsumoto[3], Hikaru Morisue[3], and Yoshiaki Toyama[3]

[1]Department of Applied Chemistry, School of Science and Technology, Meiji University, 1-1-1 Higashimita, Tama-ku, Kawasaki, 214-8571, Japan
[2]Department of Chemistry, Faculty of Science and Engineering, Sophia University, 7-1 Kioi-cho, Chiyoda-ku, Tokyo, 102-8554, Japan
[3]Department of Orthopedic Surgery, School of Medicine, Keio University, 35 Shinanomachi, Shinjuku-ku, Tokyo, 160-8582, Japan

* Corresponding author: mamorua@isc.meiji.ac.jp

Abstract: There are a rapidly increasing number of patients with diseases of their hard-tissue on the current demographic trends for old people to increase. In order to provide the aged with a high quality of life (QOL), we have developed novel scaffolds which will promote hard-tissue regeneration. We have developed porous scaffold for tissue engineering of bone using the single-crystal apatite fibers. The resulting apatite-fiber scaffolds have large pores with diameters of 110-250 μm and high porosities of 98-99%. The scaffolds were biologically evaluated using two kinds of cells, osteoblastic cells (MC3T3-E1) and rat bone marrow cells. In both cases, the cells cultured in the scaffolds showed excellent cellular response, such as good cell proliferation and enhanced differentiation into osteoblasts. We conclude that such scaffolds with high porosity and large pore size may be effective as the matrix of tissue engineered structures for promoting regeneration of bone.

Introduction

Tissue engineering is an important technology that encourages regeneration of the defecting tissue utilizing scaffolds, cells and growth factors. In the case of tissue engineering for bone, porous calcium-phosphate ceramics are generally used as scaffolds, together with bone marrow cells and rhBMP-2 or TGF-β, as reported by Ogushi and co-workers in detail [1].

Among the above three factors, the scaffold play a role of three-dimensional (3D) matrices for cells. In general, porous bioceramcis, such as hydroxyapatite ($Ca_{10}(PO_4)_6(OH)_2$; HAp) and tricalcium phosphate ($Ca_3(PO_4)_2$; TCP) have been used as a matrix for bone regeneration. Many researchers are trying to develop the high-performance scaffolds with high porosity, interconnected pores, and excellent biocompatibility.

We have also developed novel scaffolds using the apatite fibers which are synthesized by a homogeneous precipitation method [2,3]. The current apatite fibers were of single crystals with the *c*-axis orientation parallel to the long axis of the fiber [4].

Utilizing the sintering of individual fibers, we fabricated sheet-shaped scaffolds for tissue engineering of bone [5]. It has already been found that the apatite-fiber scaffold (AFS) has an excellent cellular response, such as enhanced allkaline phosphatase (ALP) activity. However, the pore size was too small to culture the cells three-dimensionally.

We have partly modified the fabrication process using carbon beads of about 150 μm in diameter as pore forming agents, in order to enlarge the pore size of the AFS. As a result of the trial, we could be successfully fabricated the AFS with large interconnected pores of 100-250 μm in diameter and high porosities of 98-99% [2,3].

In addition, we have clarified the interactions of the 3D AFSs with osteoblasts using two kinds of cells, that is, MC3T3-E1 of an osteblastic cell line and the rat bone morrow cell (RBMC) as a mesenchymal stem cell model. Actually, we examined the cellular responses to AFSs: cell attachment, proliferation, differentiation (assays and gene expression of differentiation makers of the osteoblasts), and morphology.

In this paper for key note lecture in ABC2006, we will review i) fabrication of AFS and its characterization and ii) biological properties on the basis of *in vitro* evaluation using osteoblasts.

Materials and Methods

Fabrication process of apatite-fibre scaffold and its characterisation.

The AFSs were fabricated on the basis of previous reports [2,3]. The process is briefly described as